Grant Number: DE-FG02-10ER46732 / DE-SC0004929
Recipient: Arizona State University
Title of Award: "Structural Studies of Amorphous Materials by Fluctuation Electron Microscopy"
PI: M. M. J. Treacy
Date of Report: 6/7/2018
Period Covered: 8/1/2010 – 7/31/2017

Summary
Fluctuation Electron Microscopy (FEM) is a technique that examines the fluctuations in electron scattering across a uniformly thin amorphous sample. The statistics of the intensity fluctuations, mean and variance, reveal any underlying medium-range order present in the structure.

The goals of this project were: (1) To determine the fundamentals of the scattering physics that gives rise to the variance signal in fluctuation electron microscopy (FEM); (2) To use these discoveries to find ways to quantify FEM; (3) To apply the FEM method to interesting and technologically important families of amorphous materials, particularly those with important applications in energy-related processes.

Excellent progress was made in items (1) and (2). In stage (3) we did not examine the metamict zircons, as proposed. Instead, we examined films of polycrystalline and amorphous semi-conducting diamond.

Significant accomplishments are:

(1) A Reverse Monte Carlo procedure was successfully implemented to invert FEM data into a structural model. This is computer-intensive, but it demonstrated that diffraction and FEM data from amorphous silicon are most consistent with a paracrystallite model. This means that there is more diamond-like topology present in amorphous silicon than is predicted by the continuous random network model.
(2) There is significant *displacement decoherence* arising in diffraction from amorphous silicon and carbon. The samples are being bombarded by the electron beam and atoms do not stay still while being irradiated – much more than was formerly understood. The atom motions cause the destructive and constructive interferences in the diffraction pattern to fluctuate with time, and it is the time-averaged speckle that is being measured. The variance is reduced by a factor m, $4 \le m \le 1000$, relative to that predicted by kinematical scattering theory.
(3) Speckle intensity obeys a gamma distribution, where the mean intensity $\bar{I}$ and m are the two parameters governing the shape of the gamma distribution profile. m is determined by the illumination spatial coherence, which is normally very high, and mostly by the displacement decoherence within the sample.
(4) Amorphous materials are more affected by the electron beam than are crystalline materials. Different samples exhibit different *disruptibility*, as measured by the effective values of m that fit the data.
(5) Understanding the origin of the displacement decoherence better should lead to efficient methods for computing the observed variance from amorphous materials.

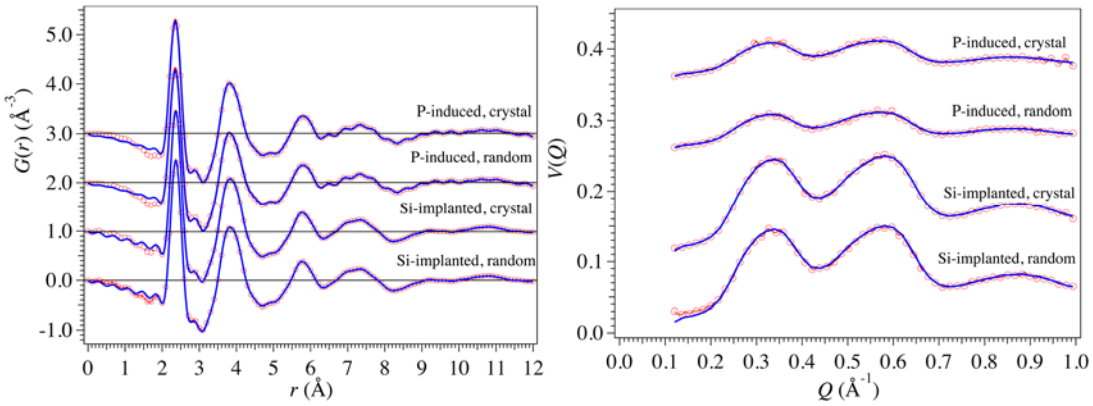

Figure 1: Left: Reduced pair distribution functions $G(r)$ for experimental data from amorphous silicon (solid blue line) and for models obtained by structural relaxation (red circles). For both the Si-implanted and pressure-induced amorphous samples, models were obtained by starting from random atomic configurations and from unfaulted cubic crystalline structures. In all four cases, the agreement between model and data is excellent. For clarity, the three upper plots are displaced vertically by offset increments of 1 Å^{-3}. Right: Normalized variance distribution functions $V(Q)$ for experimental data (solid blue line) and for models obtained by experimentally constrained structural relaxation (red circles). As for the reduced pair distribution functions, the agreement between models and data is excellent. In these plots, the model variance was scaled so that the area under each curve matched that for the data. For clarity, the three upper pairs of plots are displaced vertically by a constant offset of 0.1.

Accomplishments

(1) Reverse Monte Carlo studies of Fluctuation Electron Microscopy and Diffraction data.

It is hard to develop a direct method for inverting variance data into a structure. Since variance depends on the square of intensity, which in turn depends on atom-pair correlations, then variance depends on pair-pair correlations. Such correlations have too many degrees of freedom to solve directly.

Both the electron diffraction data and the FEM variance data were used as input experimental constraints in a computer program that adjusts the atom locations in a model so as to minimize the differences between the experimental and simulated data. The Tersoff potential for Si was also applied as a third constraint to ensure chemically reasonable local bonding. The atom moves are made randomly. The move is evaluated according to the standard Metropolis algorithm; if it improves, the fit is kept; otherwise the probability that it is kept is determined according to a pseudo-Boltzmann factor. This depends on a pseudo-temperature that is applied to the model. We refer to this method as Experimentally Constrained Structural relaxation, ECSR.

In collaboration with a group at the Australian National University and at Monash University, we applied our ECSR method to a series of amorphous silicon samples that were prepared in different ways [4,6,8]. The samples were: Si-ion implanted amorphous silicon; pressure-induced amorphous silicon. Two additional samples were the thermally annealed variants. It is remarkable that the diffraction patterns, and hence the pair distribution functions, of all four samples are essentially identical (see Figure 1, left). However, the variance plots (Figure 1, right) are significantly different, indicating that the medium-range order is different between the four samples. (The annealed plots are omitted in Figure 1.)

The ECSR code generated distinct models for the four materials. The as-prepared materials exhibited significant crystalline topology, whereas the annealed samples showed no crystalline topology at length scales greater than about 0.5 nm.

A section from the model for the Si-implanted material (not relaxed) is shown in Figure 2. It is oriented so as to reveal one of the several ordered regions that occur. These ordered regions are paracrystalline, in the sense that they are topologically ordered with the cubic silicon structure but are also strained. The annealed samples do not show any paracrystallinity and appear essentially similar to the tangled regions outside the paracrystallite in the figure.

In this study, we defined an atom as being part of a paracrystalline cubic Si structure if it exhibited the same topological "vertex symbol" as that for cubic Si. Essentially, the vertex symbol lists the size and number of the circuits that loop back to that atom. Since a tetrahedrally-coordinated atom has six inter-vertex angles, there are at least six distinct pathways that loop back to the atom, leaving along one bond, but returning along a different bond. In many instances, there are multiple paths for each intervertex angle. Every atom in cubic diamond has the vertex symbol, $6_2 \cdot 6_2 \cdot 6_2 \cdot 6_2 \cdot 6_2 \cdot 6_2 \cdot 6_2$, involving a total of 28 neighboring atoms that are visited by the circuits. This means that every intervertex angle has two distinct shortest paths, each involving six atoms, including the central atom. We defined a Si atom in the amorphous structure to be paracrystalline if it has the $6_2 \cdot 6_2 \cdot 6_2 \cdot 6_2 \cdot 6_2 \cdot 6_2 \cdot 6_2$ vertex symbol involving exactly 28 neighbors.

Figure 2 shows one of the paracrystalline models that emerged from our ECSR analysis of the as-implanted (un-annealed) amorphous Si. The red atoms each have vertex symbol $6_2 \cdot 6_2 \cdot 6_2 \cdot 6_2 \cdot 6_2 \cdot 6_2 \cdot 6_2$, and so this represents a significantly-sized paracrystallite.

The presence of paracrystallinity in amorphous Si was already strongly suspected from our prior studies, based on labor-intensive comparison of data with simulations based on inspired models. The significance of the ECSR result is that the paracrystallinity in the model emerged naturally

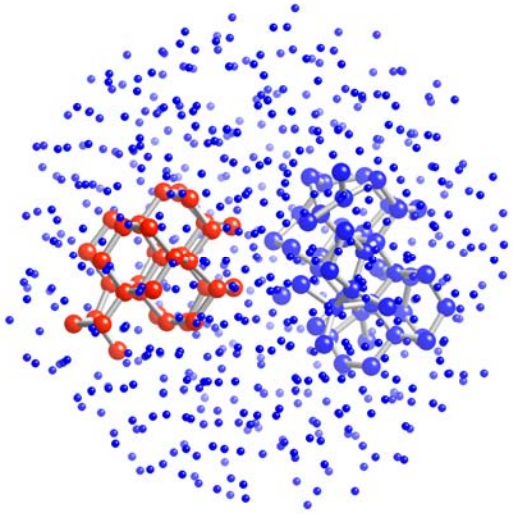

Figure 2: Paracrystalline model of amorphous silicon. The red bonded region shows a strained cubic silicon paracrystallite embedded in a matrix of disordered silicon (unbonded blue dots). The paracrystallite is viewed close to the cubic [110] direction. The region of blue bonded atoms is also disordered and illustrates more clearly the bonding disorder. The model diameter is about 2 nm.

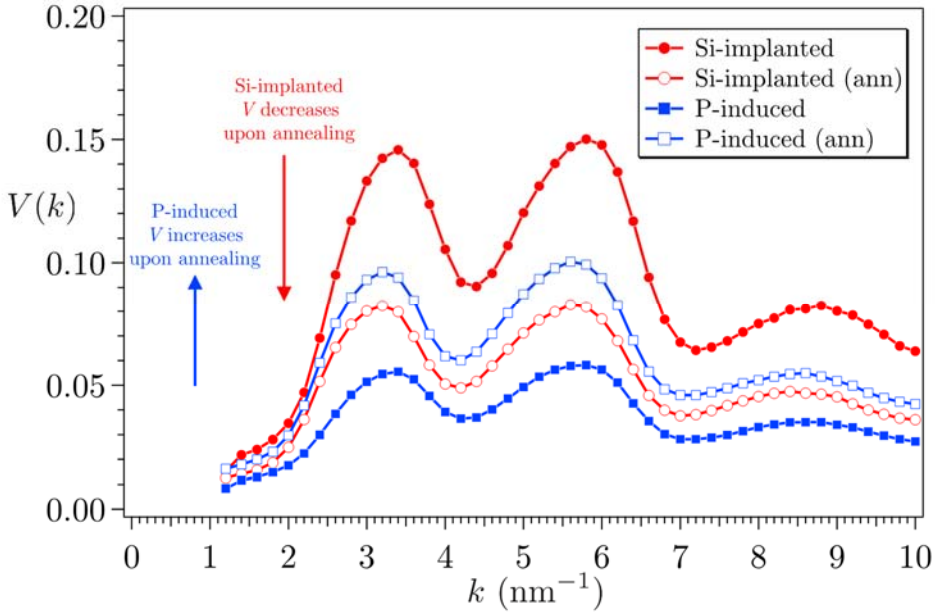

Figure 3: Plots of normalized variance for four types of amorphous silicon. Two amorphous materials were prepared from single crystal Si by: Si-implantation; high indentation pressure. These two samples were also annealed, to produce two distinct materials. The variance for the Si-implanted material is highest and is *reduces* upon annealing (red curves). The variance of the pressure-induced material is low but *increases* upon annealing. The variance plots for the two annealed materials are similar, suggesting that the annealed structure is a type of attractor state for amorphous Si.

from the data, without any user bias. This elevates our confidence about our previous conclusions and in the validity of our approach.

A curious observation arose when examining the two basic types of amorphous silicon, as shown in Figure 3. The as-prepared Si-implanted amorphous silicon (solid red circles) exhibits pronounced peaks, which are suppressed by annealing (red open circles). Conversely, the as-prepared pressure-induced amorphized sample exhibits low variance (solid blue squares). Upon annealing, the variance *increases* (open blue squares) and closely matches that for the annealed pressure-induced sample. This suggests that the annealed samples are closely similar, whereas the as-prepared materials are quite different. This suggests that this state could be the *attractor state* for amorphous silicon, generally reached by annealing.

Further, as will be discussed in more detail later, the low overall variance of the pressure-induced sample indicates that the material is more *disruptible* by the electron beam, suggesting that it is more metastable material than is the Si-implanted material.

There was one puzzling outcome from this study: the observed normalized variance was a factor of about 12 – 20 smaller than the calculated variance. Kinematical diffraction theory of electron sis pretty good, and this anomaly could not be explained. It was handled by simply introducing an additional parameter that scaled the mean experimental variance to match the mean computed variance. At the time of this study, we suspected that *incoherence* in the electron illumination was the likely source of the discrepancy. As we show in section 5 below, we later realized that it is *displacement decoherence*, arising within the sample, that is the source.

In summary, in collaboration with Dr. Borisenko at Oxford, we have confirmed that as-prepared amorphous silicon contains a high density of paracrystalline material – that is, small regions that are 1 – 2 nm in diameter that contain strained cubic silicon (Fig. 2). The size and density of paracrystallites diminish when the amorphous silicon film is annealed below the recrystallization temperature to an attractor state, but they do not disappear entirely.

(2) Void models

Our paracrystallite model is not widely accepted by the x-ray community, who rely on high resolution diffraction to obtain radial distributions functions. Roorda and Lewis (S. Roorda, L. J. Lewis, Comment on "The local structure of amorphous silicon". *Science* 338, 1539-b (2012); www.sciencemag.org/cgi/content/full/338/6114/1539-c) questioned our ECSR results, which contradicted an earlier x-ray and neutron diffraction study and which resulted in an exchange in *Science*. As pointed out above, sample-averaged diffraction alone is insensitive to medium-range order but is very effective at probing the averaged short-range order. We are confident in the correctness of our claim, because ordered regions are observable in diffraction when a 0.5 nm probe is scanned around the thinned sample. One possibility for the discrepancy is that the film surfaces tend to recrystallize, producing a stronger effect in the thin films used in electron microscopy. However, there is no evidence for such surface relaxation when cross section samples are examined.

It is an important maxim in science that "we must not fool ourselves and adhere too strongly to preferred theories." Accordingly, we devoted some considerable effort to exploring other models for amorphous silicon that might explain the observed data, but which might contradict the ECSR results. particularly those containing voids, which others have claimed also satisfy the FEM data (P. Biswas, R. Atta-Fynn, D. A. Drabold, Reverse Monte Carlo modeling of amorphous silicon. *Phys. Rev. B* **69**, 195207 (2004).)

According to K. Laaziri et al., (Phys. Rev. B 60, 13520 (1999)), each silicon atom in amorphous silicon has a coordination of 3.88 atoms. For tetrahedral materials, this means that about one atom out of every eight is missing. A missing atom is a void, of sorts, but do the missing atoms aggregate to form larger voids?

We conjectured that the computer-generated void model of Biswas *et al* is deceptive. It seemed plausible that the void surfaces might be providing easy nucleation sites for paracrystallites in their computer-generated models, and so their models could be paracrystalline after all. We prepared a set of periodic void models that contained 1728 silicon atoms per cell. After six months of computational relaxation of the models, no paracrystallites emerged, despite the fact that excellent agreement with both diffraction data and variance data were obtained. This was a bewildering result as it is hard to understand how variance peaks at the cubic-silicon 111, 220 and 311 reflections can be created by voids. We found that;

The void models show medium-range order, *but no short-range order*. Although this result satisfies the data, it is hard to understand how such a structure can be legitimate. This emphasizes the fact that, although our reverse Monte Carlo method constrains the possible space of models much better than does diffraction alone, it still leaves open the possibility of non-physical models. The paracrystallite model remains the most physically reasonable model.

This void study is inconclusive and no publication has been submitted. Atomic vacancies must be present in amorphous silicon, but it is still not clear how they are arranged, if at all. They could be present at the paracrystallite surface boundaries. This study is ongoing.

(3) Computational study of polycrystalline silicon.

It appears likely that the paracrystallites in amorphous silicon are distributed within a disordered matrix. To explore this idea, we examined simulated electron microdiffraction patterns from models of thin polycrystalline silicon [3].

The models were made by a Voronoi tessellation of random points in a box. The Voronoi domains were randomly selected to contain either a randomly-oriented cubic crystalline grain or a region of a random network material. The microdiffraction simulations from coherent probes of different widths were computed at the ideal kinematical limit, ignoring inelastic and multiple scattering. The scattered intensity variance fluctuations were found to increase monotonically with the percentage of crystalline grains in the material, which was expected. Unexpectedly, anomalously high variance was observed for models that approached 100% crystalline grains with no imperfections. This was attributed to scattering interference terms between adjoining grains, generating a type of super-variance.

We confirmed that the reduced normalized variance, $V(k) - 1$, that is associated with four-body correlations at scattering vector *k*, varies inversely with specimen thickness. Further, for probe sizes *R* larger than the mean grain size, we confirm that the reduced normalized variance obeys the predicted form given by Gibson et al. (*Ultramicroscopy*, 83, 169–178; 2000) for the kinematical coherent scattering limit.

Although FEM is in principle a quantitative experimental method, in exactly the same sense that high-resolution imaging and electron diffraction are quantitative, it has been difficult so far to come up with a straightforward analytical procedure to process the data to obtain a model. It is not sufficient to measure lattice spacings, or index reflections. A physical model is needed to

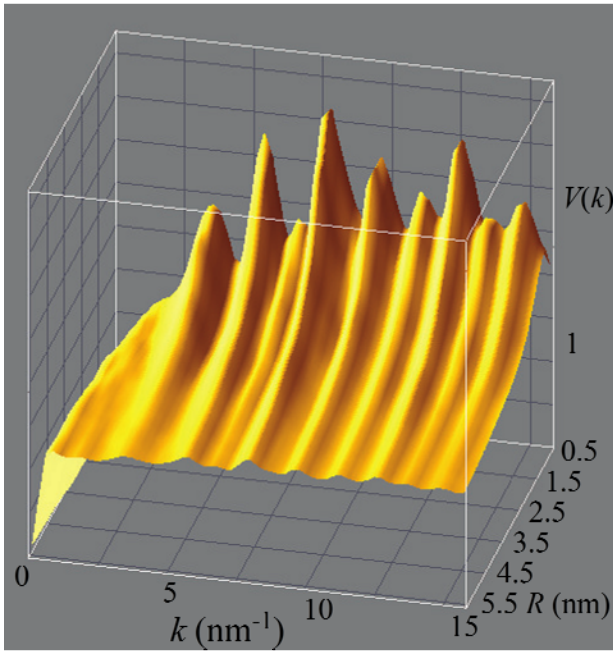

Figure 4: Three-dimensional plot of the calculated normalized variance, *V*(*k*), as a function of scattering vector *k* and microscope resolution, *R*. The mean paracrystalline grain size is 1.2 nm. The variance is a maximum near R ≈ 0.8 nm, which is the value of Λ for this model. For $R > \Lambda$ the variance decays approximately as R^{-2}, as the model predicts for this regime. These plots do not compensate for decoherence effects, and so the baseline normalized variance equals 1.0.

explain FEM data. The reverse Monte Carlo method described in section (1) goes a long way towards remedying this issue, but that requires vast computational resources.

Although FEM is quantitative, some of the contributions to the speckle contrast were still poorly understood. In particular, the normalized variance is typically about one to three orders of magnitude less than that expected from simple kinematical scattering. Important progress has been made towards understanding the origin of this speckle contrast suppression, which we refer to as *decoherence*. Our progress in this area is described in more detail in a later section.

A detailed computational analysis of the statistics of scattering from granular materials confirms that an earlier model relating normalized variance to a characteristic length scale of medium-range order, Λ, and the scattering vector is essentially correct. We showed that the normalized variance $V(k,R)$, as a function of scattering vector *k* and resolution *R* is

$$\frac{1}{V(k,R)-1} = \frac{a}{\Lambda} + \frac{b}{\Lambda^3}R^2,$$

where *a* and *b* are constants. Plots of $\left[V(k,R)-1\right]^{-1}$ vs. R^2 give straight lines whose slope and intercept give Λ.

A computational model (Fig. 4) confirms that this equation is valid provided $R > \Lambda$, i.e. that the microscope resolution (controlled by the objective aperture size) is greater than the characteristic length scale of the medium-range ordering. This asserts one of the more paradoxical results of FEM – that the technique works best at low resolution.

An important step forward for quantifying the effects of thickness and decoherence on the normalized variance was made by identifying the invariant quantity

$$\left[mV_m(k;t)-1\right]t = \text{constant}.$$

$V_m(k;t)$ is the normalized variance at scattering vector *k* for a sample thickness *t*, where $t > \Lambda$. *m* is a parameter that characterizes the incoherence/decoherence. This useful relation allows us to compute the variance for the simpler *m*=1 case, and thinner sample, t_1, and apply

$$V_m(k;t) = \frac{1}{m}\left(\frac{t_1}{t}\left[V_1(k;t_1)-1\right]+1\right).$$

The computation of $V_1(k;t_1)$ for *m*=1, and a much thinner model, t_1, would appear to provide a way to speed up the simulation of the desired quantity $V_m(k;t)$ considerably. Although the above equation now seems obvious with hindsight, it remained elusive for over a decade. The significance is that this equation allows a significant speedup of variance computations for thicker samples, while potentially compensating for the effects of decoherence, which are governed by the parameter *m*. The deeper significance of the parameter, *m*, will be revealed in section 5.

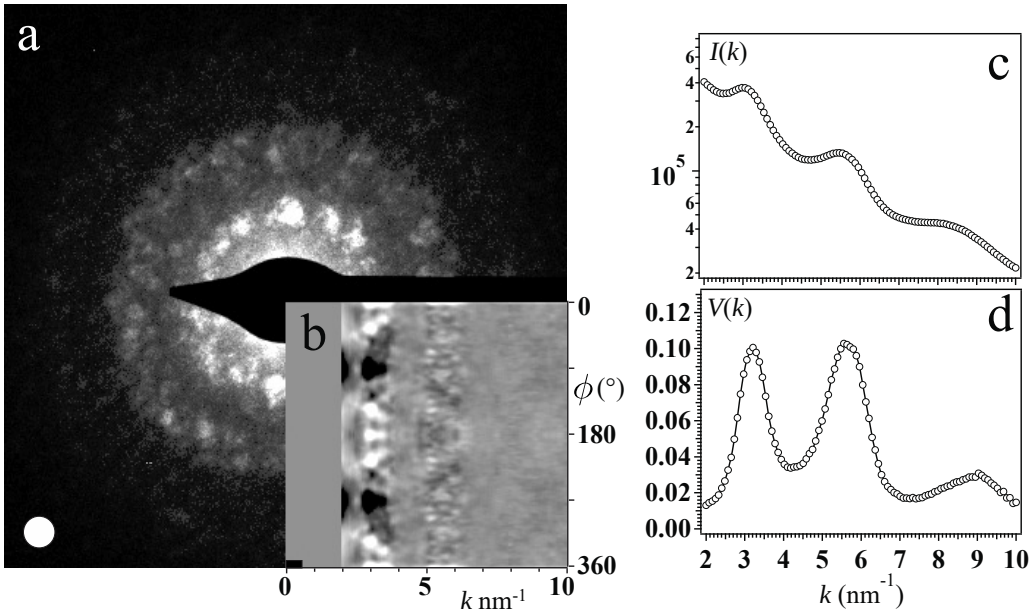

Figure 5: (a) Typical electron coherent nanodiffraction pattern from the 20-nm thick amorphous silicon film using a probe of nominal resolution 2.3 nm. (b) The associated correlograph. The scattering vector k for both the nanodiffraction pattern and correlograph are aligned on the plot. The vertical axis on the correlograph represents the azimuthal angle ϕ. (c) Logarithm of the azimuthally-averaged mean diffracted intensity versus k for 200 nanodiffraction patterns. (d) Normalized variance plot for this sample, showing the three signature peaks confirming the presence of paracrystallinity.

(3) Correlographs: An alternative method for determining structural correlations within diffraction data.

P. Wochner et al (Proc. Natl. Acad. Sci. U.S.A. 106, 11 511, 2009) had earlier presented an x-ray study indicating that five-fold, and odd-numbered axial symmetries were observed in focused x-ray probe studies of latex-sphere samples. Our earlier studies using fluctuation x-ray microscopy of similar samples did not see such symmetries.

We undertook to repeat the methodology (which had been proposed earlier by Clark, Ackerson and Hurd, Phys. Rev. Lett. 50, 1459, 1983) in the TEM on an amorphous silicon sample [1].

A perfectly coherent electron probe was focused to various probe sizes between about 0.3 nm to 8 nm and FEM diffraction data were collected as usual. In addition to computing the normalized variance, the normalized autocorrelation function along the azimuthal axis, ϕ, was calculated for each diffraction pattern,

$$G(R, \boldsymbol{r}_p, k, \phi) = \frac{\langle I(R, \boldsymbol{r}_p, k, \phi) I(R, \boldsymbol{r}_p, k, \phi + \Delta) \rangle_\Delta}{\langle \langle I(R, \boldsymbol{r}_p, k, \phi) I(R, \boldsymbol{r}_p, k, \phi + \Delta) \rangle_\Delta \rangle_\phi} - 1.$$

Here, Δ is a dummy variable representing integration over the full 360° azimuthal angle for an angular offset of ϕ.

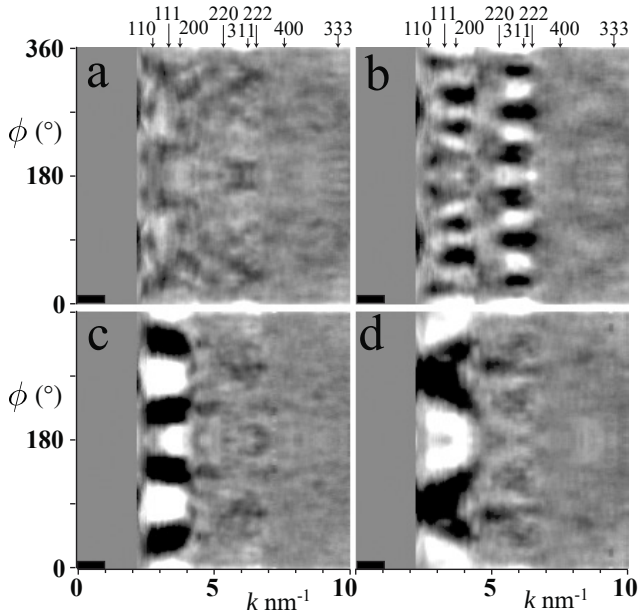

Figure 6: Typical correlographs taken from four probe positions on the sample for a probe resolution 1.0 nm. Correlographs are highly variable between scanned points and tend to show strong features near scattering vectors corresponding to strong Bragg reflections, *hkl*, of crystalline cubic silicon. Strong correlations can also occur near forbidden reflections such as 110 and 200. The uniform grey band on the left is from the beam stop. The semiangle subtended by the illumination disk along the k axis is indicated by the black bar.

Figure 5 outlines the procedure. A diffraction pattern is acquired (Fig 5a). The angular correlation is made, and then the azimuthal angle is unwrapped and placed on the *y* axis. The radial component of the scattering vector is laid along the *x* axis (Fig 5b). The logarithm of the mean diffraction profile, and the normalized variance are also presented in Figs 5c and 5d.

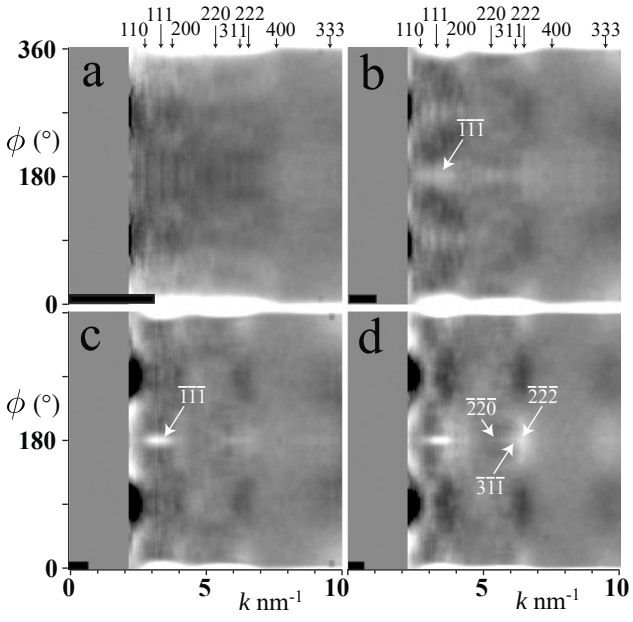

Figure 7: Mean correlographs, averaged over 200 probed positions for four different probe resolutions, R. (a) R = 0.3 nm. (b) R = 1.0 nm. (c) R = 1.5 nm. (d) R = 2.3 nm. The high-resolution correlograph, (a), shows little correlation. The lower-resolution correlographs (b), (c), and (d) show strong 180° Friedel correlations between the 111 and $\overline{111}$ peaks, and the 222 and $\overline{222}$ Friedel peaks. The semiangle subtended by the illumination disk is indicated by the horizontal black bars.

Figure 6 shows typical correlographs obtained from different locations within the sample. Strong indications of 2-fold and six-fold symmetry appear in some of the patterns, which were less obvious in the original diffraction patterns.

Figure 7 shows the sample-averaged correlographs for four different electron probe sizes. A strong 2-fold symmetry appears, with indications of a strong Friedel peak at the $\overline{111}$ and $\overline{222}$ positions (i.e. at the 180° line for the 111 and 222 reflections) for the larger probe sizes. This probably arises because larger probes have a smaller range of incident angles at the sample. Any strong diffracted peak, at hkl will tend to produce a strong Friedel peak at $\overline{hkl}$ provided the scattering angles are small. A strongly convergent probe (i.e. small probe) will have only a small region in the Friedel condition because of the curvature of the Ewald sphere.

The data in Figure 7 were matched to simulations and were found to be consistent with a structure that has about 10% paracrystalline Si in a disordered matrix – an observation that is evident in the individual diffraction patterns.

(4) Speckle Statistics: A model for the speckle intensity distribution.

For random speckle in an image, with a fixed mean intensity, intensity is expected to be distributed as a negative exponential [7, 10],

$$P(I) = \frac{1}{\bar{I}} \exp\left(-\frac{I}{\bar{I}}\right).$$

$\bar{I}$ is the mean intensity. This result suggests that the most common intensity encountered in an image pixel is zero. Puzzlingly, zero is almost never observed experimentally. The negative exponential model arises for exactly the same mathematical reasons as does the Boltzmann distribution in quantum mechanical systems, which is also a negative exponential. If we have an image of (say) 1000×1000 pixels, with a mean intensity of (say) 100 counts per pixel, there is only one arrangement in which all 10^6 pixels get exactly 100 counts. However, suppose we allow

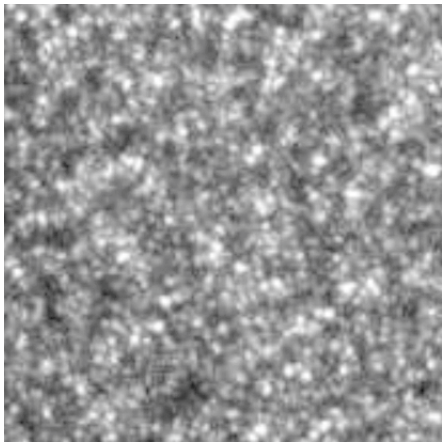

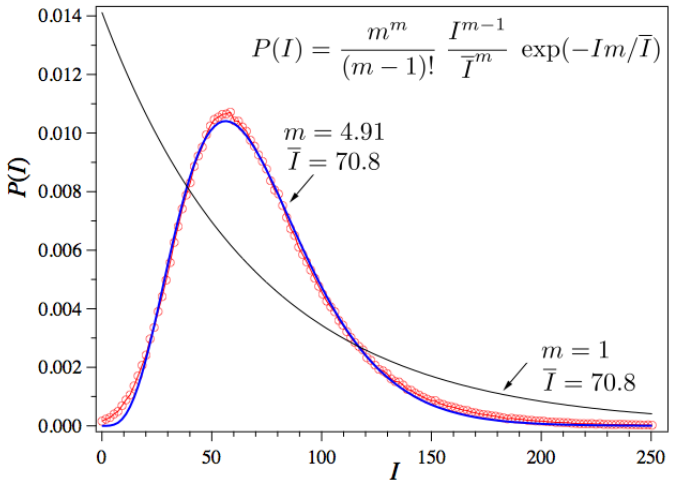

Figure 8: Left: Speckle in a tilted dark-field image of amorphous carbon. Right: Typical speckle statistics from similar images (red circles). The blue curve is a fit to the gamma distribution, where the equation itself is presented in the graphic. The fit to the gamma distribution is remarkably good. The meaning of the parameter *m* was once thought to relate to the number of incoherent sources in the illumination. It is now realized that it relates to the decoherence induced by the scattering processes in the sample, such as beam damage and multiple scattering. For comparison, the idealized negative exponential curve is also shown (black line).

one pixel to have 101 counts with another pixel getting just 99 counts, and all others remain at 100 counts, we have 10^6 possible locations for the pixel with 101 counts, and $10^6 - 1$ locations for the pixel with 99 counts, giving a total of $\sim 10^{12}$ arrangements. Clearly, if all that we know of the image is the mean intensity, then the likelihood that all pixels are the same value, 100, is close to zero. Of course, intensities can be any distribution, provided the mean intensity is constrained. The negative exponential is obtained by maximizing the informational entropy consistent with the mean intensity $\bar{I}$. By far, the most common arrangement of intensities under this sole constraint has a negative-exponential intensity histogram (see solid line in Fig 8).

In practice, we observe the distribution shown in red points in Figure 8. We found that we could match this curve to a gamma distribution (the equation is shown in Figure 8), where an additional parameter *m* is required as well as the mean intensity $\bar{I}$. We originally argued that the parameter *m* represented spatial incoherence in the probe. A fully coherent probe would have *m*=1, whereupon the gamma distribution gives the negative exponential as before. Experimental observations show that values of *m* range between about 4 and 1000, values that are inconsistent with the known probe coherence, which would give *m* values closer to 1.0.

The negative-exponential distribution is never observed in FEM experiments. For a random speckle distribution with incoherent illumination, the variance is 1/*m*. The normalized variance background gives us a way to estimate the *m* value of our materials.

It was a longstanding puzzle as to why the measured *m* value was usually one to three orders of magnitude less than the known incoherence parameter. This puzzle emerged in part 1 of our study. Since the illumination coherence corresponded to values of *m*≈1, we needed to identify another source for the parameter *m*.

(5) Displacement decoherence: An explanation of the anomalously low normalized variance seen in experiments.

An exhaustive study was made of amorphous Si and amorphous C, with variable fluence, fluence rates, voltage and thickness [10].

The normalized variance was found to decrease with increasing voltage and increasing fluence, suggesting that a damage mechanism might be at work.

A number of models were considered, including beam damage, energy losses, large amplitude vibrations and multiple scattering. Excellent matches to the data were obtained from a physically unlikely model – for atomic vibration amplitudes of about 0.15 nm. This length scale is comparable to the Si-Si bond length (0.235 nm) and is therefore not physically realistic. However, it is telling that such an extreme phonon vibration model gives normalized variances that match the data qualitatively. Remarkably, the continuous random network (CRN) model gives no peaks when the atoms are stationary, but reproduces the peaks (locations and relative amplitudes) in the data quite well when the vibration amplitude is large. The paracrystallite model also reproduces the data well, as expected. Additional modeling revealed that the large vibrational amplitude, plus multiple scattering, accounts for the experimental data well. The big surprise is that the CRN model also reproduces features in the data.

The vibration model is clearly unphysical. However, it appears to represent well the averaged effect of motions within the sample. For example, an electron may displace an atom, or break a bond, causing a larger section of material, with many atoms in it, to tilt. Although the individual motions are small, many atoms are affected.

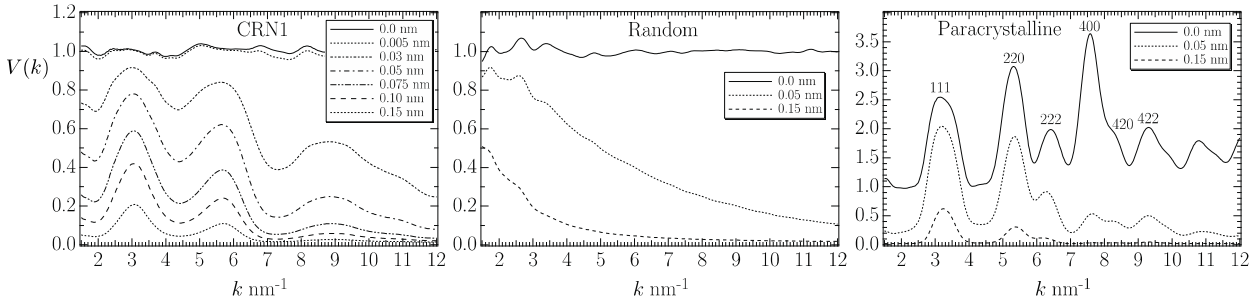

Figure 9: Computed normalized variance for three models of amorphous silicon. Left, a continuous random network model. Center, a randomize-location atomic model. Right, a paracrystalline model. In each model atoms are given a Gaussian vibration amplitude, with standard deviations of 0 to 0.15 nm. Curiously, the CRN model (left) shows no peaks when atoms are stationary, but peaks appear as the vibration amplitude is increased, matching the experimental data in location, but the amplitude is still too high. A random model (center) shows no peaks. The paracrystalline model (right) starts off with peaks that are too strong at zero vibrational amplitude, but also matches the data at larger vibration amplitudes. Clearly, a vibration amplitude of 0.15 nm is about 60% of a bond length and is not physically realistic. However, it is clear that the variance suppression is equivalent to such a vibration amplitude.

As noticed in section 1, Figure 3, amorphous materials appear to be more sensitive to the beam than crystals. Different amorphous Si samples appeared to have different *disruptibilities*.

What appears to be happening is that during the acquisition of data in the CCD camera the samples moves about. The constructive and destructive interferences flicker rapidly over time and are therefore averaged out during the data acquisition time. This, in effect, adds a large incoherence to the data. It mimics spatial incoherence in the illumination, but is actually arising from atomic motion during the data acquisition. Its effect on the speckle intensity histogram is identical to that from incoherence, and it contributes large values of m, suppressing the normalized variance, which scales as $1/m$. We refer to this effect as *displacement decoherence*.

Modeling displacement decoherence is computer intensive. We are still working on finding a method to emulate it rapidly. This is important if we want the reverse Monte Carlo studies of section 1 to be free of the simple scaling parameter. We now know how to compute the variance suppression, but the present methods are impractical for Monte Carlo simulations.

(5) A surprise in the First Born approximation. Principal collaborator, Dirk van Dyck, (University of Antwerp)

The first Born approximation states that the scattered electron wavefunction from an atom is

$$\psi(\mathbf{r}) = e^{i\mathbf{k}.\mathbf{r}} + \frac{f(\mathbf{q})}{\lambda}\frac{e^{ikr}}{r}$$

$f(\mathbf{q})$ is the electron scattering factor, $\mathbf{k}$, the propagation wavevector, and λ is the electron wavelength. Since an atom is a weak phase object, we might have expected this equation to actually be

$$\psi(\mathbf{r}) = e^{i\mathbf{k}.\mathbf{r}} + i\frac{f(\mathbf{q})}{\lambda}\frac{e^{ikr}}{r}$$

The factor of i giving the "correct" phase. I could not find an explanation for this apparent discrepancy, and many textbooks in fact present the second form.

Even more baffling is the fact that the *Optical Theorem* predicts that the first form has zero total scattering cross section – clearly incorrect! Nobody could resolve this puzzle for me, so, in collaboration with Dirk van Dyck, we reported this surprise in the journal Ultramicroscopy [5].

This article (as hoped) brought us an explanation for the mystery from M. Lentzen in Jülich. Although the last term of the First Born approximation looks like a spherical Huygen's wavelet (in the near-field), leading us to conclude (erroneously) that there is a missing phase. However, it is modified by $f(\mathbf{q})$, meaning that it is not a near-field term, but is in fact a far-field term. In other words, 1Å behind the atom, the wavefront is already in the far-field! The phase is indeed not i.

It is satisfying to have this mystery resolved, since it relates intimately to the kinematical scattering theory that is used to compute the FEM variance.

There is an amusing outcome related to this publication. I have received multiple requests from medical journals to write more on this topic. It was several years before I realized that they think the topic is about first-born children!

(6) Interferometric diffraction from amorphous bilayers

To examine the effect of sample thickness on the normalized speckle variance, we attempted several methods to get accurate control of sample thickness. This was surprisingly difficult. The best we could do was to use the micro-manipulator in a focused ion beam (FIB) machine to roll the sample into a tube with several layers of thickness and to then break the film so that we had multiple layers overlapping of identical thickness. The layer thickness was determined from the edge view of the rolled specimen and so we had up to six well-controlled thicknesses, including zero thickness (see Fig. 10) [11].

Remarkably, diffraction patterns from doubled layers in particular had fringes resembling Newton's rings (Fig 11). The fringes arose because the doubled layers were not in contact in all places. The gap between the two plane layers gave rise to interference between the diffracted

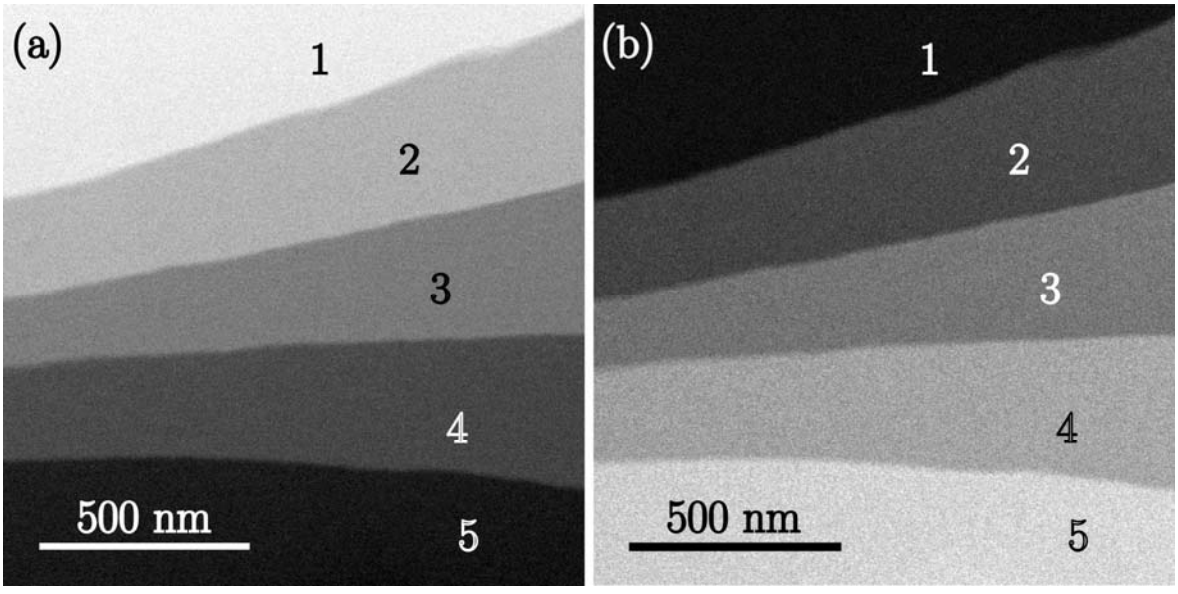

Figure 10: Terraces on carbon that are exactly 30 nm increments in thickness. Left, STEM bright field image; Right, STEM annular dark-field image. The region labelled "1" is a hole in the sample.

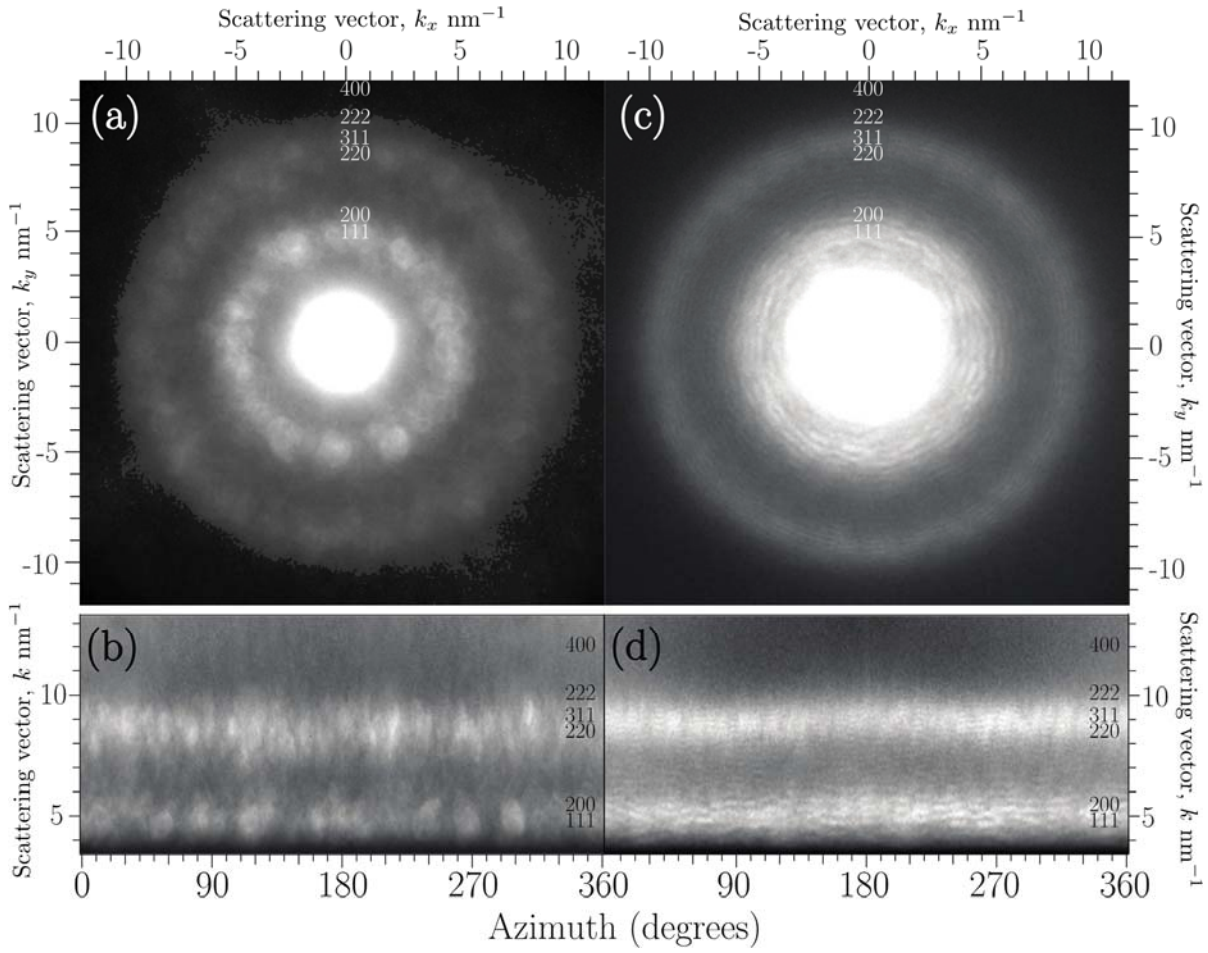

Figure 11: Left top. Diffraction pattern from a single 30-nm thick layer of amorphous carbon. Top right. Diffraction from two overlapping layers of amorphous carbon. Note the large speckles in the former, and the concentric fringes in the latter. Bottom. These are the same as the diffraction patterns above, but unwrapped so that the vertical axis is the radial wavevector, and the bottom is the 360° range of the azimuthal angle.

waves from each film.

This artifact gave us an excellent opportunity to measure directly the temporal coherence of the waves between the two layers, as well as a direct measure of the decoherence as a function of the scattering wavevector. Fringes disappeared when the layers were separated by more than a micron, consistent with known values of the coherence length in a LaB_6 filament at 200 kV. Fringe intensity faded quickly with increasing wavevector k, confirming that the decoherence contributes a strong Debye-Waller type term that annihilates coherence above $k \geq 10$ nm^{-1}.

This is not say that the vibration amplitudes are literally as large as 0.15 nm, as inferred in section (5). Instead, this result confirms that the aggregate sample motions (vibrations, local tilts, beam damage, etc) act analogously to an average vibration amplitude of 0.15 nm.

Publications supported by the grant (All of these papers have been published)

(1) J. M. Gibson, M. M. J. Treacy, T. Sun and N. J. Zaluzec,
Substantial crystalline topology in amorphous silicon,
Physical Review Letters **105** 125504 (2010).

(2) M. M. J. Treacy,
Z Dependence of Electron Scattering by Single Atoms into Annular Dark-Field Detectors,
Microscopy and Microanalysis **17** 847–858 (2011).

(3) M. M. J. Treacy and J. M. Gibson,
Examination of a polycrystalline thin-film model to explore the relation between probe size and structural correlation length in fluctuation electron microscopy.
Microscopy and Microanalysis **18** 241–253 (2012).

(4) K. B. Borisenko, B. Haberl, Amelia C.Y. Liu, Y. Chen, G. Li, J. S. Williams, J. E. Bradby, D. J. H. Cockayne, M. M. J. Treacy,
Medium-range order in amorphous silicon investigated by constrained structural relaxation of two-body and four-body electron diffraction data,
Acta Materiala **60** 359–375 (2012).

(5) M. M. J. Treacy and D. Van Dyck,
A Surprise in the First Born Approximation for Electron Scattering,
Ultramicroscopy **119** 57–62 (2012).

(6) M. M. J. Treacy and K. B. Borisenko,
The Local Structure of Amorphous Silicon,
Science **335** 950–952 (2012).

(7) M. M. J. Treacy,
Speckles in Images and Diffraction Patterns,
Handbook of Nanoscopy, Ed. by Gustaaf van Tendeloo, Dirk van Dyck, and Stephen J. Pennycook, Ch 12 , 405–435 (2012).

(8) M. M. J. Treacy and K. B. Borisenko,
Response to Comment on "The Local Structure of Amorphous Silicon,"
Science **338** 1539 (2012).

(9) T. Sun, F. A. M. Koeck, A. Rezikyan, M. M. J. Treacy and R. J. Nemanich,
Thermally enhanced photoinduced electron emission from nitrogen-doped diamond films on silicon substrates,
Physical Review B, **90** 121302(R) (2014).

(10) A. Rezikyan, Z. Jibben, B. A. Rock, G. Zhao, F. A. M. Koeck, R. F. Nemanich, and M. M. J. Treacy,
Speckle Suppression by Decoherence in Fluctuation Electron Microscopy,
Microscopy and Microanalysis **21** 1455–1474 (2015).

(11) A. Rezikyan, J. A. Belcourt and M. M. J. Treacy
Interferometric Diffraction from Amorphous Bilayers,
Microscopy and Microanalysis **21** 1348–1360 (2015).

(12) J. M. Gibson and M. M. J. Treacy,
Fluctuation Microscopy Analysis of Amorphous Silicon Models,
Ultramicroscopy **176** 74–79 (2017).

(13) S. M. Collins, R. K. Leary, P. A. Midgley, R. Tovey, M. Benning, C.-B. Schönlieb, P. Rez and M. M. J. Treacy,
Entropic Comparison of Atomic-Resolution Electron Tomography of Crystals and Amorphous Materials,
Phys. Rev. Letts. **119** 166101 (2017).